Hindawi
Advances in Polymer Technology
Volume 2022, Article ID 3830961, 14 pages
https://doi.org/10.1155/2022/3830961

Research Article

Numerical Simulation of Grounding Characteristics and Temperature Field of Mine Tires under Multiple Working Conditions

Jinquan Guo,[1] **Peng Ding**,[1] **Jianhong Gao**,[1,2,3] **Zhenhua Huang**,[4] **Qiyan Guo**,[4] **and Xiaoxiang Yang**[1]

[1]*Fuzhou University, School of Mechanical Engineering and Automation, Fujian Fuzhou 350108, China*
[2]*Quanzhou Normal University, School of Chemical Engineering and Materials, Fujian Quanzhou 362000, China*
[3]*Xinhe New Materials Co., Ltd, Fujian Quanzhou 362000, China*
[4]*Haian Rubber Group Co., Ltd, Fujian Putian 351254, China*

Correspondence should be addressed to Jianhong Gao; gaojh@qztc.edu.cn

Received 14 September 2022; Revised 2 November 2022; Accepted 17 November 2022; Published 15 December 2022

Academic Editor: Gyorgy Szekely

Mine tires are an essential and expensive component of heavy mining machinery. This study explored the grounding characteristics and temperature field distribution of mining tires during driving as well as the relationships between the maximum temperature and tire inflation pressure, load, and speed. Two-dimensional and three-dimensional finite element models of mine tires were established. Steady-state rolling simulation analysis was conducted based on inflation and static load simulations. Temperature field simulation analysis was conducted with the tire section as a research object. The accuracy of the finite element model was verified. Analysis results demonstrated that the grounding contact area decreased with an increase in charging pressure and increased with an increase in load. With an increase in inflation pressure, the maximum normal grounding stress increased in the middle part of the tread and decreased near the shoulder. The maximum normal grounding stress continuously deviated in the shoulder direction with an increase in load. Temperature field analysis indicated that the tire had the maximum temperature at the binder position, where the first belt layer was connected to the second belt layer, which corresponds to the maximum stress position in the steady-state rolling simulations. Tire temperature increased with driving speed. The maximum temperature increased with an increase in tire deflection, whereas the deflection decreased with an increase in inflation pressure and increased with an increase in load. Speed had the greatest influence on the maximum temperature, followed by load, with inflation pressure having the smallest influence. The results of this research can be used to improve the service life of mine tires to improve productivity and reduce costs.

1. Introduction

In the mining industry, the use of heavy mining machinery helps reduce costs and increase productivity. This has resulted in the development of huge mining trucks and radial tires with outer ring diameters of more than 3 m [1]. The usage environment of mine tires is harsh, resulting in high loads, short service life, and extreme prices. Therefore, investigating methods to extend the service life of mine tires is crucial. According to previous studies, mining tire failure is primarily due to high shoulder temperature, resulting in local shoulder voids and cracking, which ultimately leads to tire failure [2]. Therefore, investigating the grounding characteristics and temperature field distribution during steady-state rolling of mining tires is not only of great significance for design and use but also lays the foundation for fatigue life research at different temperatures.

Currently, the principal research approaches in the tire temperature field are experimental testing methods and numerical simulation methods [3]. In comparison to experimental methods, numerical simulations cannot only reduce design costs but also reduce the duration of the development

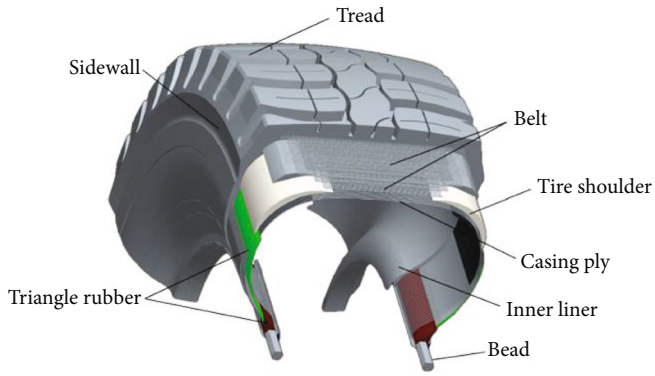

Figure 1: Schematic of tire construction.

process [4]. Additionally, experimental testing systems for the interior temperature distributions of mine tires have not been fully developed. Numerous simulation and experimentation studies have demonstrated[3–7] that tire temperature fields can be examined using finite element simulations. Using the results of stress strain or strain energy density curves obtained from steady-state rolling analysis, Marais and Venter [8], Cho et al. [9], Lin and Hwang [10], and Wu et al. [11] calculated the heat generation rate of rubber elements based on static load and steady-state rolling simulations of passenger car tires; temperature fields were simulated for two-dimensional sections. Yin et al. [12] and Song et al. [13] simulated the temperature fields of three-dimensional tire models using the same methodology. Their research demonstrated that the gap between simulation results and experimental results was less than 8%, confirming the viability of their method. However, because the size of a mine tire is significantly greater than that of a passenger car tire and the weight is correspondingly greater, this simulation approach is susceptible to the convergence problem. Beyond the limited research on the temperature fields of mine tires conducted by Wedam Nyaaba over the past two years, few studies have employed this method to investigate the temperature fields of large mine tires.

This study considered a mine tire as a research object. A two-dimensional slice of the tire was considered to conduct finite element simulations of its temperature field. During steady rolling, the grounding condition, maximum temperature, and temperature distribution were investigated in the simulations. A three-dimensional finite element model of the tire was also developed.

The remainder of this paper is organized as follows. Section 1 discusses the establishment of finite element models for mine tires. Section 2 presents the simulation analysis procedure used to evaluate the established model. Section 3 presents the orthogonal experimental design adopted in this study, and Section 4 presents our analysis results. Finally, Section 5 summarizes our study and concludes this paper.

2. Establishment of Tire Finite Element Models

2.1. Tire Geometry and Finite Element Models. A tire has a composite structure with rubber and steel wires serving as the primary force components. The steel wire and rubber tire components are presented in Figure 1. There are 11 distinct rubber materials, including rubber for tire treads, sidewalls, shoulders, belts, and triangles. The skeleton component consists of one to six layers of steel wire embedded in corresponding rubber materials such as tires and belts.

As shown in Figure 2, the structural design of the tire enables the creation of a two-dimensional axisymmetric model with steel wire elements in (b) and rubber elements in (a). Using diverse materials, the rubber components are divided into 12 separate sections. Because the rim is significantly rigid than the tire, it is characterized as a rigid body and assigned a reference point. ABAQUS was used for the finite element analysis of the tires, and a total of 1505 elements were set to rubber material, containing 1659 nodes, and the element type was CGAX4H/CGAX3H. There were 482 elements set as steel wire material, containing 489 nodes, whose element type is SFMGAX1.

A three-dimensional tire model was constructed using the two-dimensional model as a foundation. The two-dimensional axisymmetric model was rotated along the circumferential direction in increments of 4° about its axis of symmetry to generate 90 parts. The resulting three-dimensional model contained 149,310 elements and 135,450 nodes, and the element types were C3D8H and C3D6H. Because the main purpose of this study was to explore the internal temperature distribution of tires and the tire pattern has little effect on the internal temperature, the tire pattern was not established in this study. In addition, other minor details inside the tire that would not affect the simulation results were removed.

ABAQUS's rebar element command was used to bury the skeleton steel wire element inside the equivalent rubber element. For improved convergence during model calculation, ensuring that each rubber element is embedded with a single rebar element is vital. To imitate the wire cord arrangement in a real belt layer, the cross-sectional area of the rebar elements, distance between neighboring wires, and angles relative to the meridian direction can be specified.

2.2. Material Parameters. The rubber compounded of tread, casing, inner liner, belt, sidewall, and triangle rubber was offered by Haian Rubber Group Co. Ltd. Experiments were conducted to obtain the following key material properties: (1) hyperelasticity, (2) viscoelasticity, and (3) thermal parameters.

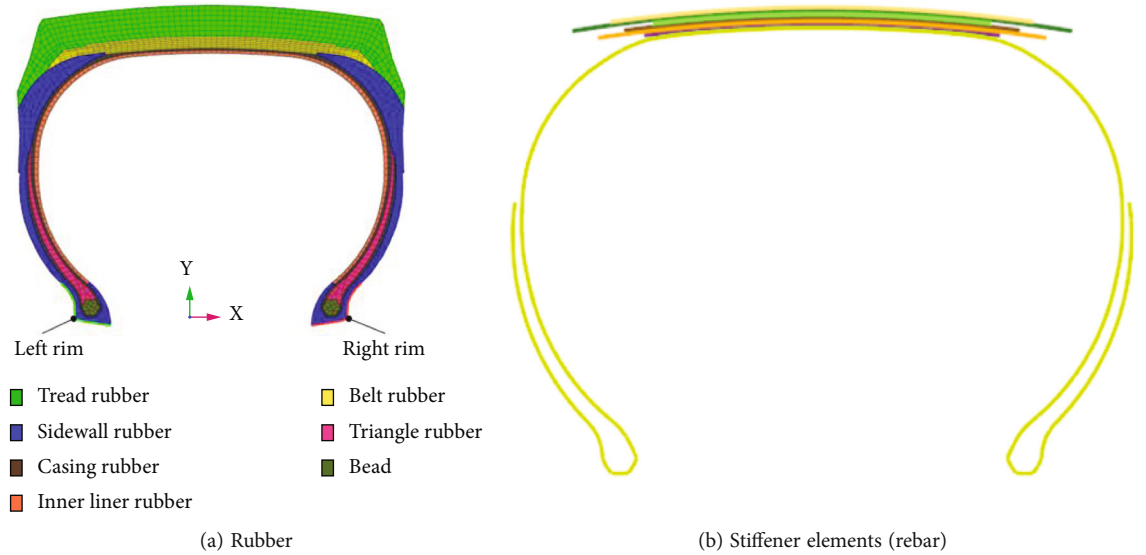

(a) Rubber (b) Stiffener elements (rebar)

Figure 2: Tire model based on two-dimensional axisymmetric finite elements.

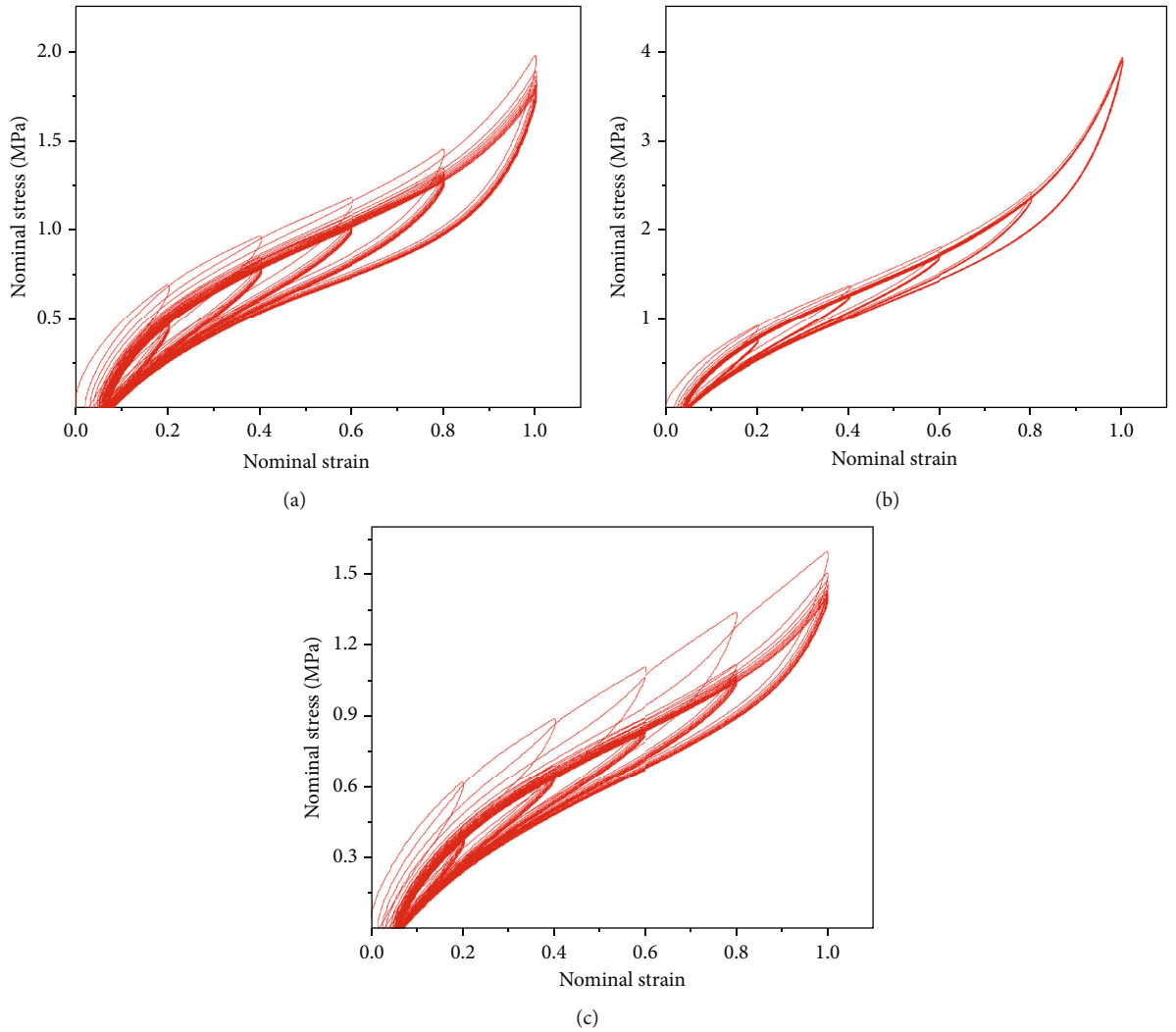

Figure 3: Stress-strain cycle stretch curve under five strains of (a) Tread rubber, (b) Body rubber, and (c) Side rubber.

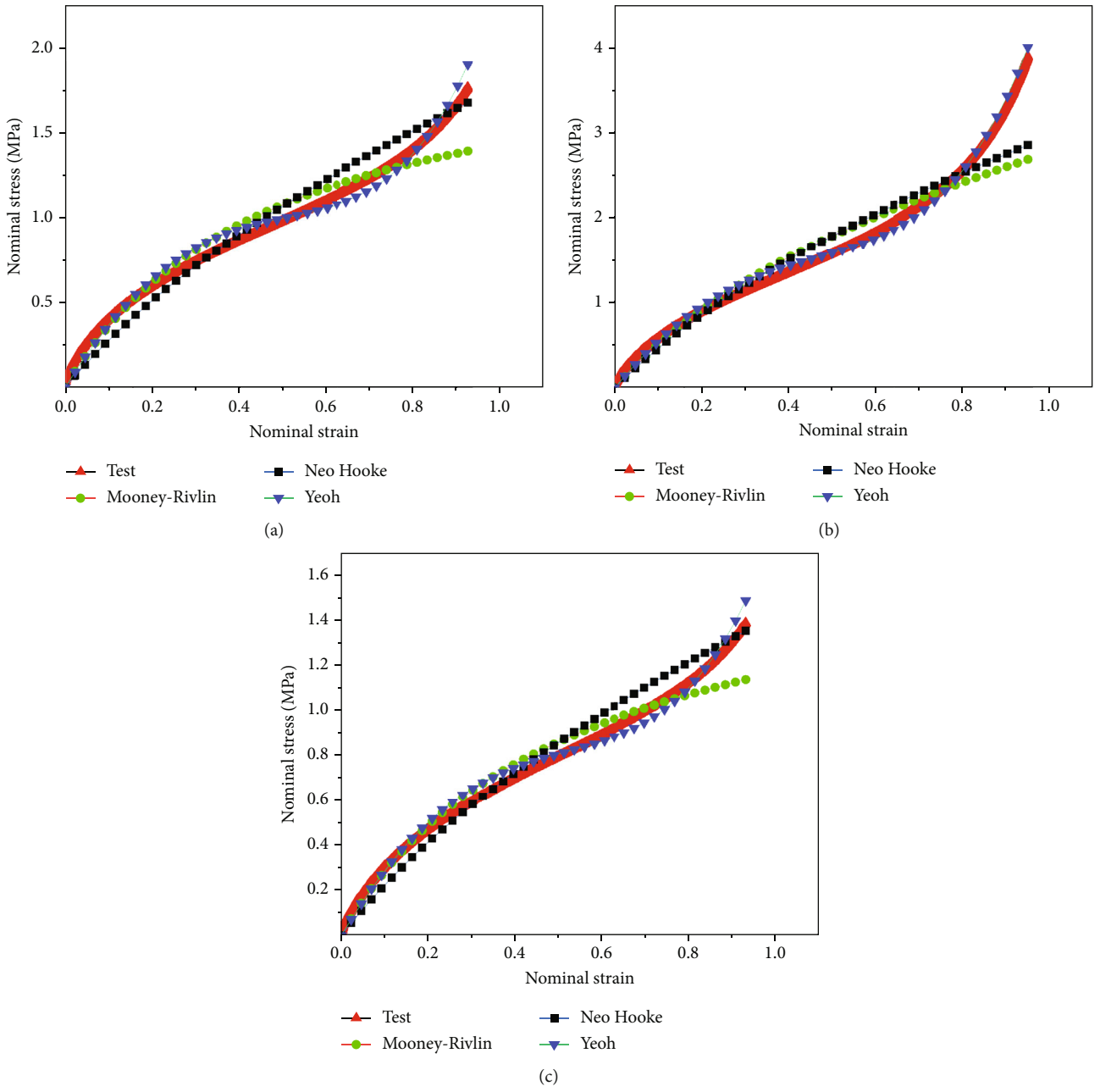

Figure 4: Three constitutive models fitted for (a) Tread rubber, (b) Body rubber, and (c) Side rubber.

2.2.1. Hyperelasticity Property Parameters. Using a Shimadu AG-X Plus electronic universal testing system, the stress-strain relationships of all tire rubber compounds were analyzed. The specimen was type I dumbbell-shaped with a thickness of 2 mm, and the length of the experimental section was 20 mm. The experimental rate was 50 mm/min; the noncontact extensometer was used to obtain the experimental section displacement. To eliminate the Mullins effect of the rubber material, the specimen was loaded and unloaded multiple times under five strains (0.2, 0.4, 0.6, 0.8, and 1.0) until the curve reached a stable state, and the cycle loading curve of tread rubber, sidewall rubber, and carcass rubber is shown in Figure 3. Taking the last loading curve as the experimental curve, the first-order Mooney-Rivlin model, the first-order neo-Hooke model, and the third-order Yeoh model were used to fit the experimental data. Figure 4 presents the fitting results for the tread rubber, side rubber, and body rubber. Evidently, the Yeoh model provides the best fit. Therefore, the Yeoh hyperelastic material model was utilized to characterize the materials. The material characteristics of each rubber component are listed in Table 1.

The Yeoh model [14] expression for the strain energy density function is

$$W = C_{10}(I_1 - 3) + C_{20}(I_1 - 3)^2 + C_{30}(I_1 - 3)^3, \quad (1)$$

Table 1: Constitutive parameters of the Yeoh model for each rubber compound.

	C_{10} (MPa)	C_{20} (MPa)	C_{30} (MPa)
Tread	0.613	-0.122	0.029
Casing	0.829	-0.212	0.067
Inner liner	0.401	-0.090	0.018
Belt	1.417	-0.589	0.232
Sidewall	0.448	-0.078	0.019
Triangle rubber	0.698	-0.196	0.060

Table 2: Parameters for the mechanical properties of steel wires.

	Young's modulus(MPa)	Poisson's ratio	Density (kg/m^3)
Belt 1	198698	0.3	7850
Belt 2 & 3	193871	0.3	7850
Belt 4	210000	0.3	7850
Belt 5 & 6	210000	0.3	7350
Body ply	193871	0.3	7850
Bead	237140	0.3	7870

where C_{10} is half of the initial shear modulus, C_{20} is the softening parameter during deformation, and C_{30} is the hardening parameter under large stress. These parameters can be obtained by fitting the uniaxial tensile experimental data, and I_1 is the first principal elongation invariant.

The tire is a composite structure composed of rubber and steel wire. Steel wire is used for No. 1–6 belt layers, body ply, and bead. The mechanical property parameters of the steel wire used in each part are shown in Table 2.

2.2.2. Thermal Parameters of Rubber. When simulating the tire temperature field, the thermal performance parameters of the rubber material need to be set. To ensure the accuracy of the simulation, the thermal expansion coefficient and specific heat of the rubber material were measured by LFA 467 flash thermal conductivator. The specimen was 10 mm × 10 mm square and 2 mm thick. The density of rubber materials was determined by the drainage method, and the thermal conductivity value of each part of the tire was calculated. Table 3 shows the thermal conductivity, specific heat, and density parameters of each material during simulation.

2.2.3. Viscoelastic Material Parameters for Rubber. Hysteresis coefficients (tanδ) were used to characterize the viscoelastic loss degrees of the rubber compounds [15, 16]. The hysteresis coefficient of the material needed to be tested and applied to the calculation of strain energy density, as shown in Section 2.3.1. When an alternating load is applied to a rubber material, the chain segment inside the material was affected by internal friction as it moves. Therefore, the movement of the chain segment cannot keep up with the external force, and in the end, the strain of the material lags behind the stress, with the hysteresis coefficients representing the degree to which the strain lags behind the stress.

Table 3: Thermal performance characteristics of rubber.

	Thermal conductivity (W/m k)	Specific heat (J/kg k)	Density (kg/m^3)
Tread	0.224	1898	1314
Casing	0.229	1722	1344
Inner liner	0.241	1830	1318
Belt	0.255	1719	1440
Sidewall	0.218	2037	1150
Triangle rubber	0.201	1725	1164

Table 4: Average hysteresis coefficients of compounds measured through testing.

	Hysteresis coefficient (tanδ)		
	0.46 Hz	0.92 Hz	1.38 Hz
Tread	0.1408	0.1301	0.1243
Casing	0.0909	0.0856	0.0828
Inner liner	0.2241	0.2274	0.2292
Belt	0.0890	0.0836	0.0806
Sidewall	0.0631	0.0607	0.0598
Bead	0.1427	0.1370	0.1338

The dynamic thermomechanical analyzer (DMA) was used to determine the hysteresis coefficients of six kinds of rubber compounds. Three rolling speeds, 7.5 k m/h, 15 m/h, and 22.5 m/h, were employed in the simulation discussed in Section 2. Therefore, dynamic thermomechanical experiments were conducted using the three corresponding frequencies, 0.46 Hz, 0.92 Hz, and 1.38 Hz, according to the rolling speeds.

Because calculating the heat generation rates of subsequent elements using the values at each temperature separately is difficult, values between 0 and 100°C should be averaged at each frequency to simplify the calculation of subsequent formulas. Table 4 lists the mean values of the compounds at each frequency.

3. Simulation Analysis

3.1. Two-Dimensional Simulation Analysis of Tire Assembly and Inflation. Analysis was performed using the axisymmetric two-dimensional finite element model introduced in Section 1. To mimic the real assembly conditions and improve convergence during calculation, the left and right rims in Figure 2(a) were shifted by 12.5 mm along the x-axis to simulate the actual rim assembly process. To simulate the tire inflation process, a fully constrained boundary condition was applied to the rim and pressure perpendicular to the inner wall was applied to the inner cavity of the tire.

3.2. Analysis of Three-Dimensional Static Loading and Steady Rolling. Static loading analysis of the 3D model was conducted using the rim-fixing method. We established a road surface beneath the tire and applied displacement and

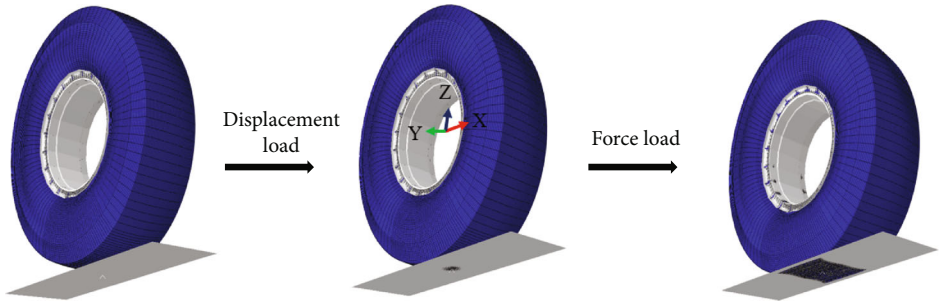

Figure 5: Schematic representation of the three-dimensional static loading process for the tire model.

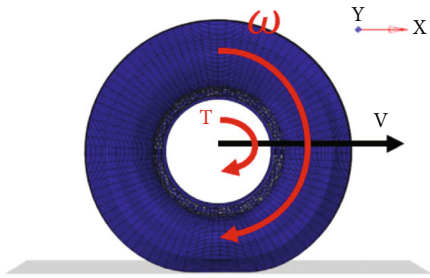

Figure 6: Schematic diagram of angular velocity and velocity imposition.

load to the road surface. The road surface was defined as a rigid body, and a reference point was established for the surface. Our analysis consisted of two steps. In the first step, a z-axis displacement was applied to the reference point of the road to make the road touch the tire. The second step involved applying a corresponding load to the road reference point. Figure 5 presents a schematic representation of the loading procedure for three-dimensional static tire loading.

The steady-state rolling analysis of the tire was carried out on the basis of the 3D static loading analysis, and the results of the static loading process of the tire are restarted in the analysis. Restarting the result file means that this rolling analysis is based on displacement control rather than force control. Applying a positive velocity v along the x -axis direction and an angular velocity ω clockwise relative to the y-axis, if the torque at the rim centroid point around the y-axis trends toward zero, it indicates that the tire is in the steady-state rolling condition. Otherwise, adjusting angular velocity until the steady-state rolling is achieved. Figure 6 presents a schematic diagram of angular velocity and velocity imposition.

3.3. Analysis of the Steady-State Temperature Field. In the steady rolling process of a tire, the tire returns to its initial position after one rotation and the variation in strain energy density in any section during a rolling period is identical. On this basis, the following hypotheses are proposed. (1) There is no temperature gradient along the circumferential axis of the tire. (2) The thermal boundary conditions of the tire along the circumferential axis are identical. Furthermore, because the viscoelastic heat generation of the rubber material is significantly greater than the friction heat generation between the tire and ground, the latter is disregarded. According to these hypotheses, for tire temperature field analysis, the three-dimensional model was converted back into a two-dimensional axisymmetric model, which was used for the analysis and calculation of the temperature field. Additionally, because the time lag of the heating wire element is significantly smaller than that of the rubber element, the rebar element was deleted and replaced with DC2D4 and DC2D3 rubber element types.

In this study, our analysis of the temperature field only employed the one-way decoupling method, meaning only the influence of tire deformation on the temperature field was considered while the influence of temperature on deformation was ignored.

3.3.1. Calculation of the Mechanisms and Rate of Tire Heat Generation. When a tire rolls in a steady state, it continuously deforms and recovers under periodic load excitation.

Table 5: Design table of orthogonal experiment of tire.

Level	Factors		
	Inflation pressure (MPa)	Load (N)	Velocity (km/h)
1	0.5	466670	7.5
2	0.55	550000	15
3	0.6	633330	22.5

Table 6: Conditions for orthogonal tire experimentation.

Working condition	Inflation pressure (MPa)	Load (N)	Velocity (km/h)
1	0.5	466670	7.5
2	0.5	550000	22.5
3	0.5	633330	15
4	0.55	466670	15
5	0.55	550000	7.5
6	0.55	633330	22.5
7	0.6	466670	22.5
8	0.6	550000	15
9	0.6	633330	7.5

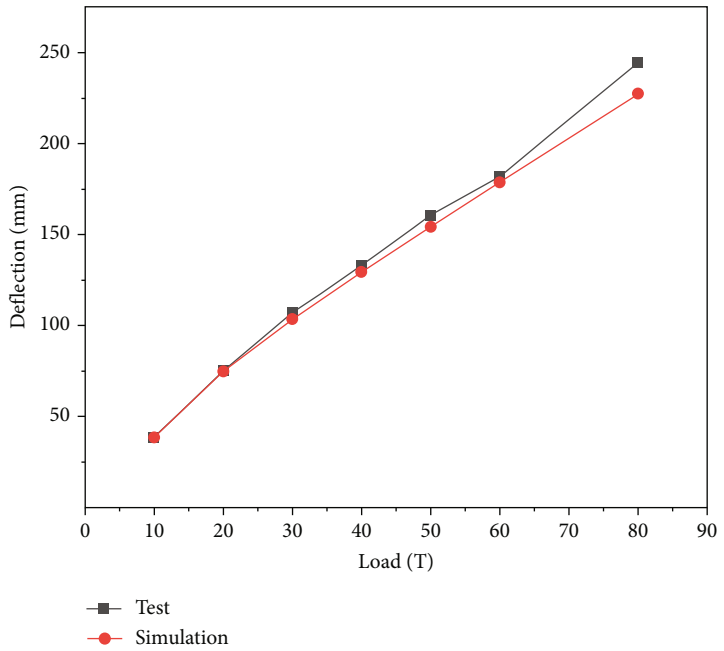

Figure 7: Comparison of simulated and experimental tire radial stiffness curves.

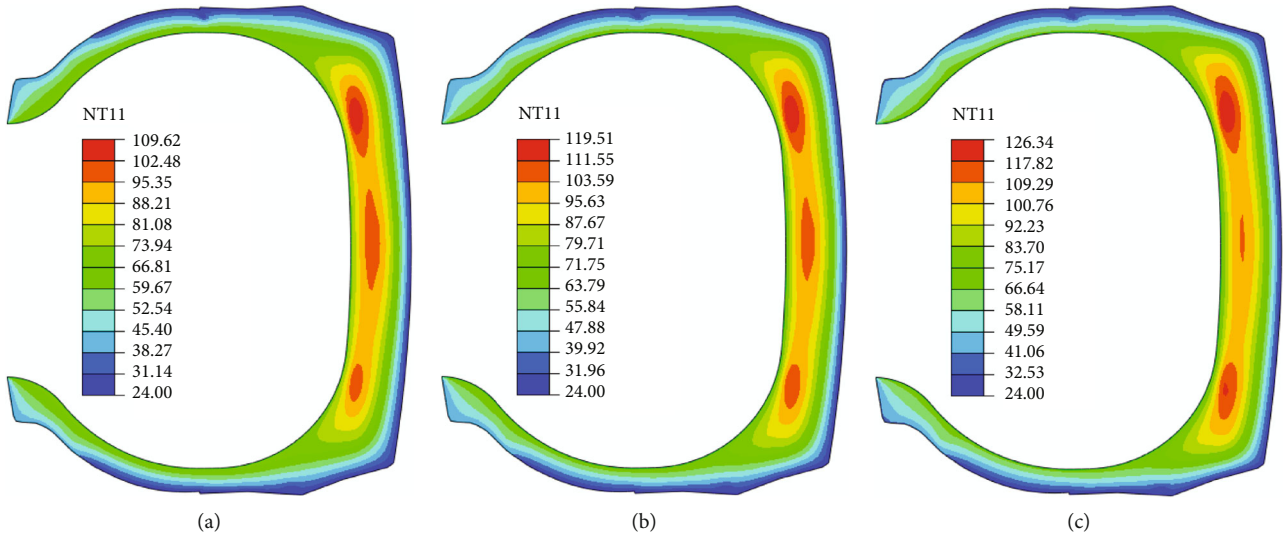

Figure 8: Tire temperature field distribution under loads of (a) 466667 N, (b) 550000 N, and (c) 633330 N when the inflation pressure is 0.6 MPa, and the speed is 15 km/h.

Based on the hysteresis of the rubber material, energy dissipation is produced during deformation and recovery, and this dissipation is eventually released as heat energy. This heat energy release is referred to as the hysteresis loss of the rubber material. The hysteresis loss is a function of the loss factor of the rubber material, and the average loss factor for each rubber material was presented in a previous paper[6].

Assuming that all of the energy generated during the tire deformation process is converted into heat energy, the dissipated strain energy density per element and cycle is [8]

$$U_{\text{loss}} = U \tan \delta. \tag{2}$$

Here, U_{loss} is the energy density of the dissipative strain in one cycle, and U is the total strain energy density over a period.

Because several components were produced by circumferential rotation during the development of the 3D tire model, the total strain energy density obtained by a rotating tire unit over one week is defined as

$$U = \sum_{i=1}^{n} \Delta U_i, \tag{3}$$

where n is the number of duplicates produced by tire rotation, and ΔU_i represents the increase in the strain energy density of the corresponding component.

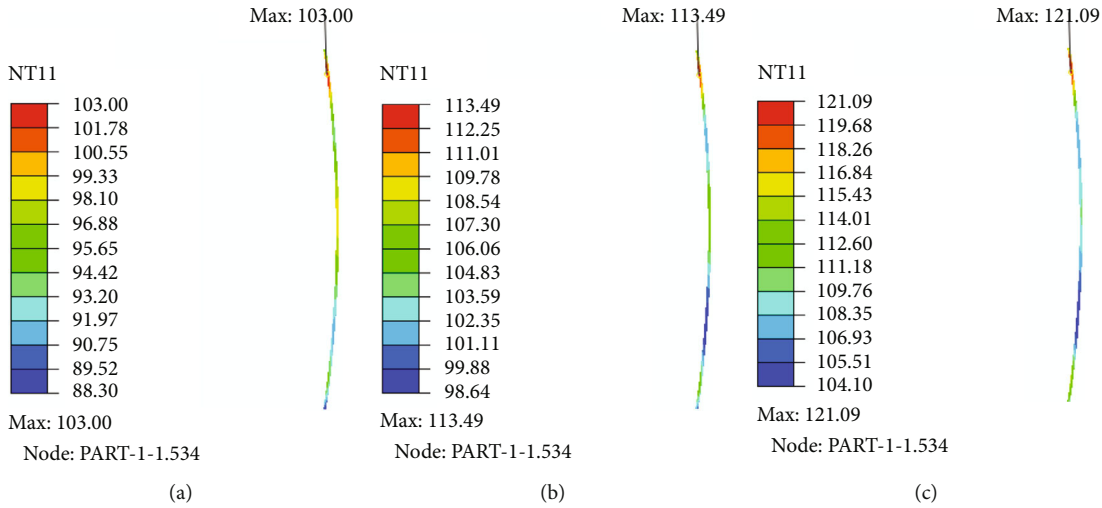

Figure 9: Temperature field distribution of tire 6# belt under loads of (a) 466667 N, (b) 550000 N, and (c) 633330 N when the inflation pressure is 0.6 MPa, and the speed is 15 km/h.

Therefore, the rate of heat production for each element is

$$Q = U_{\text{loss}}/T, \tag{4}$$

where Q is the rate of heat production per element, T is the period of constant tire rolling ($T = 2\pi R/V$), R is the tire's rolling radius during steady rolling, and V is the velocity of the tire.

Because it is necessary to calculate the heat generation rate of each rubber unit as a heat source during tire temperature field analysis, the strain energy density of each unit during steady tire rolling was extracted. The heat generation rate of each unit was calculated using a Python program based on the aforementioned formula. Using the USDFLD and HETVAL subroutines in ABAQUS, the calculated heat generation rate was assigned to the corresponding 2D finite element model elements as a heat source for temperature field analysis.

3.3.2. Analysis of Temperature Field Boundary Conditions. Theoretical and experimental research has determined that convective heat transfer is the primary factor that influences tire rolling [17]. Based on the first and third boundary conditions of heat transfer, the convective heat transfer coefficient of each part of the mine tire was investigated and a formula for calculating the convective heat transfer coefficient of each component was derived as follows [18]:

$$h_T = 2.2v^{0.84}, \tag{5}$$

$$h_i = h_r = 0.4h_T, \tag{6}$$

$$h_s = \frac{h_T - h_r}{l}\Delta l, \tag{7}$$

where h_T, h_i, h_r, and h_s are the convective heat transfer coefficients of the tire crown, inner surface, rim, and side, respectively. v is the air velocity, and l is the diameter of the side arc of the tire.

Table 7: Simulation and experimental comparison of the maximum temperature of 6# belt (0.6 MPa, 15 km/h).

Load (N)	Simulation (°C)	Test (°C)	Deviation
466670	103.00	97	6.1%
550000	113.49	112	1.3%
633330	121.09	122	0.7%

The temperature settings of each tire surface during the simulations are as follows. The external environment temperature of the tire was 25°C. When the vehicle speed was 15 km/h, inflation pressure 0.6 MPa, and load 533620 N, the air temperature in the inner cavity of the tire was 68°C after rolling for 7 h. According to the relationship between the air temperature in the inner cavity and the vehicle speed in [19], the temperature of the inner cavity of the tire at 7.5 km/h, 15 km/h, and 22.5 km/h was set to 60°C, 70°C, and 80°C, respectively. The temperature of the tire contact area with the rim was set to 40°C [17].

4. Orthogonal Experimental Design

To investigate the grounding condition, maximum temperature, and temperature distribution of the tire when it achieves steady rolling and the influence degrees of inflation pressure, load, and speed on the maximum temperature of the tire, we designed a set of orthogonal experiments. Orthogonal experimental design is a method to study multifactorial and multilevel problems, wherein representative points are selected from a comprehensive test according to orthogonality for experimentation. For the points selected, the standard working pressure is 0.6 MPa, the vehicle speed is 15 km/h, and the load is 46667–63333 kg. These values represent the majority of the load on the tire when it is working, and the temperature values under other loads can be inferred from the values of these three cases. The

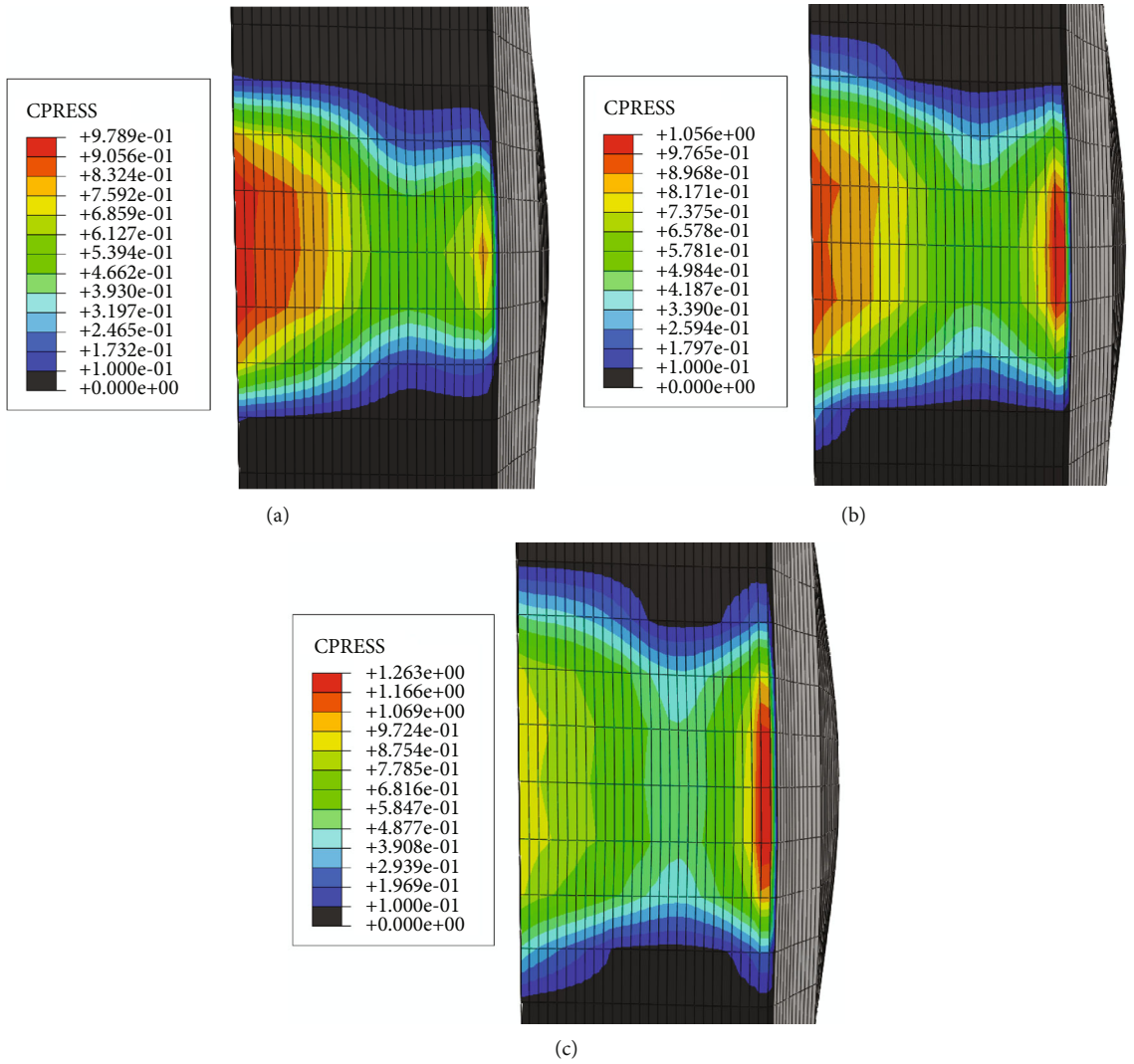

Figure 10: Grounding stress distribution of a 3D tire model under 0.5 MPa of inflation pressure under loads of (a) 466670 N, (b) 555550 N, and (c) 633330 N.

influencing factors and levels are shown in Table 5, and Table 6 lists the specific orthogonal experimental conditions.

5. Results Analysis

5.1. Finite Element Model Verification

5.1.1. Radial Stiffness Verification. Radial stiffness is the performance of a tire's ability to bear load, which is expressed as the relationship between the radial force (load) and the radial deformation (deflection) of the tire under vertical loading. When the standard inflation pressure was 0.6 MPa, a static load simulation was conducted on the mine tire under seven loads (10 tons, 20 tons, 30 tons, 40 tons, 50 tons, 60 tons, and 80 tons), and the radial stiffness curve of simulation analysis was obtained.

During the experiment, the tire load was steadily increased from 0 to 80 tons. The experimental deflection was recorded at seven loads corresponding to the simulation, and the experimental radial stiffness curve was obtained. To verify the accuracy of the simulation model, the simulated radial stiffness of tire was compared with the experimental radial stiffness. Simulation and experimental radial stiffness curves are shown in Figure 7. The experiment was completed in Haian Rubber Group Co. Ltd.

As shown in Figure 7, the tire deflection curve of the finite element simulation closely followed the experimental trend and was slightly lower than the experimental curve overall. Based on the absence of a tread pattern in the finite element model, the maximum deviation at 80 tons was only 7%. Therefore, the finite element model developed in this study is considered to be credible.

5.1.2. Validation of Tire Temperature Field Simulations. According to the method described above, under the inflation pressure of 0.6 MPa and the speed of 15 km/h, the finite element simulation analysis of the tire temperature field under three working conditions of 466670 N, 550000 N, and 633330 N loads was carried out. Figure 8 shows the temperature field simulation results of the tire under these three

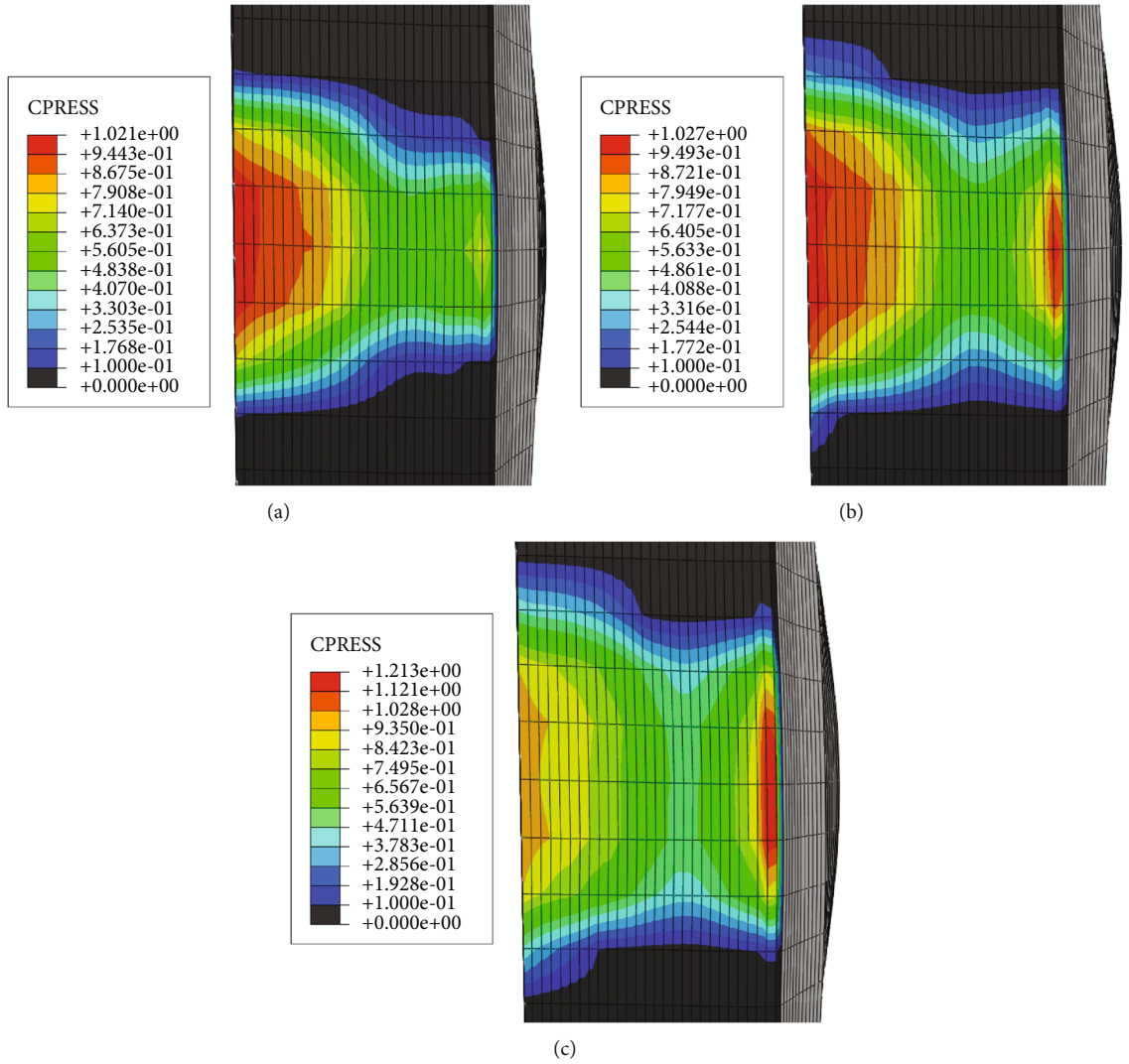

Figure 11: Grounding stress distribution of a 3D tire model under 0.55 MPa of inflation pressure under loads of (a) 466670 N, (b) 555550 N, and (c) 633330 N.

operating conditions, and it can be seen from the figure that the end of the belt had the highest temperature, followed by the middle part of the tread and the shoulder pad rubber part. The maximum tire temperature was at the junction between the end of the $1^{\#}$ belt and the end of the $2^{\#}$ belt.

To verify the accuracy of the tire temperature field simulation, rolling experiments were conducted on the drum testing machine under the same three working conditions. Before the experiment, a hole was punched from the tire tread to the end of the tire $6^{\#}$ belt, steadily rolled for 8 h, at which point the experiment was stopped, and the thermometer was immediately placed into the prepunched hole to measure the temperature at the end of the $6^{\#}$ belt. The temperature field simulation results at the end of the $6^{\#}$ belt in three conditions are shown in Figure 9. The maximum temperature of the simulation and experiment of the $6^{\#}$ belt under the three conditions is shown in Table 7, and it can be seen from the table that the maximum deviation between the simulation and experiment under the three working conditions was 6.1%.

5.2. Evaluation of Orthogonal Results

5.2.1. Evaluation of Grounding Area and Strain. The grounding stress distributions for inflation pressures of 0.5 MPa, 0.55 MPa, and 0.6 MPa are presented in Figures 10–12, respectively. One can see that when the inflation pressure remains constant, the maximum normal grounding stress and area of grounding contact both increased with the load. For example, when the inflation pressure was 0.5 MPa and the load was 466670 N, 555550 N, and 633330 N, the maximum normal grounding stress was 0.9789 MPa, 1.256 MPa, and 1.263 MPa, respectively. As the load increased, the maximum position of normal grounding stress gradually shifted from the center of the tread toward the tread's edge. When the load was 466670 N, 555550 N, and 633330 N, the corresponding grounding contact areas were 0.77 m^2, 0.84 m^2, and 0.96 m^2, respectively. Under the same load, as the inflation pressure increased, the normal grounding stress in the middle portion of the tread increased, whereas the normal grounding stress in the edge portion of the tread decreased

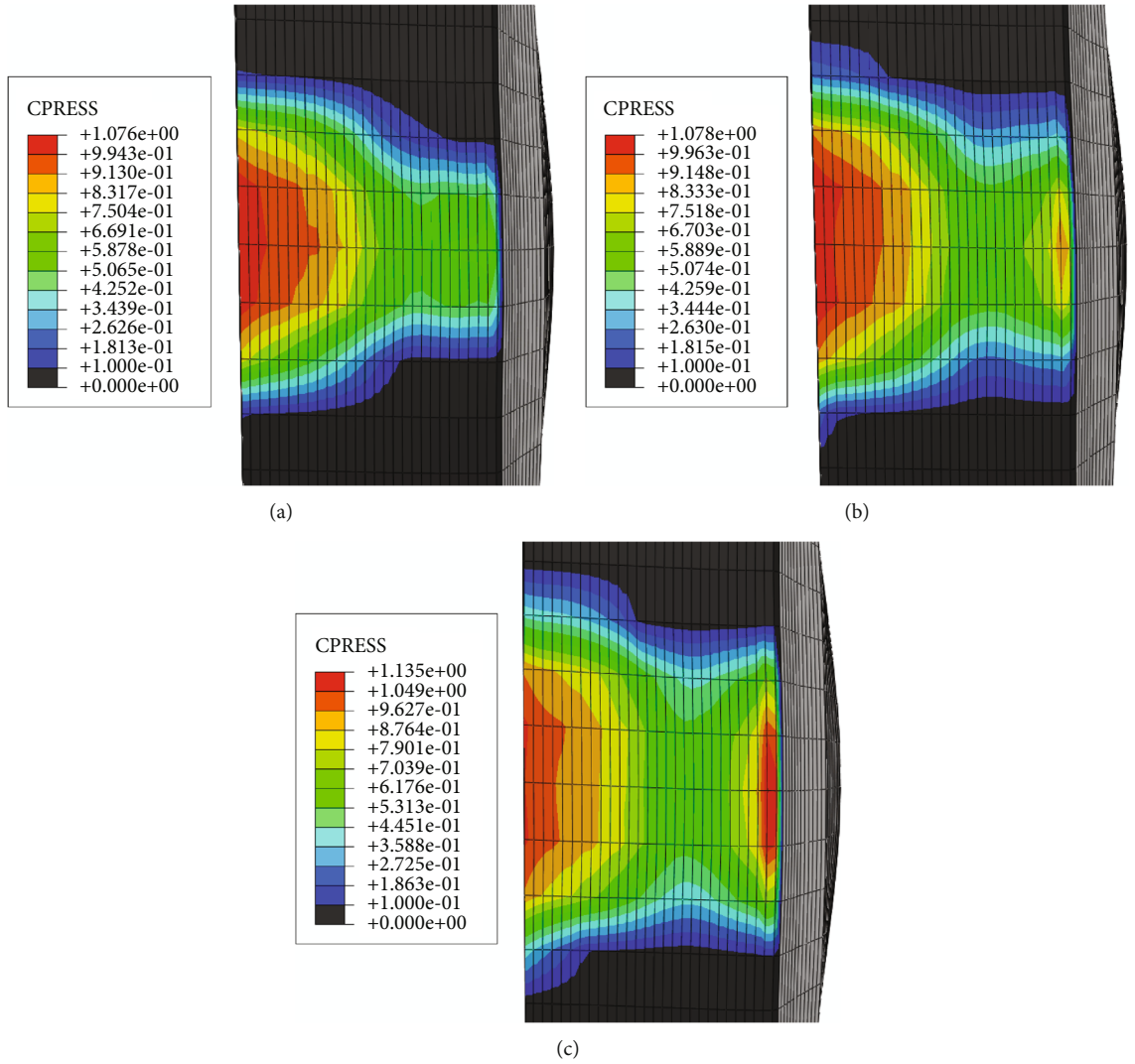

Figure 12: Grounding stress distribution of a 3D tire model under 0.6 MPa of inflation pressure under loads of (a) 466670 N, (b) 555550 N, and (c) 633330 N.

Table 8: Deflection and maximum tire temperature under identical conditions.

Working condition	Factors			Results	
	Inflation pressure (MPa)	Load (N)	Velocity (km/h)	Deflection (mm)	The highest temperature (°C)
1	0.5	46667	7.5	153.066	76.11
2	0.5	55000	22.5	174.703	155.54
3	0.5	63333	15	198.334	127.89
4	0.55	46667	15	146.252	109.48
5	0.55	55000	7.5	166.853	81.00
6	0.55	63333	22.5	187.223	170.56
7	0.6	46667	22.5	138.251	142.72
8	0.6	55000	15	157.764	119.51
9	0.6	63333	7.5	177.145	84.92

and the grounding contact area decreased. When the load was 466670 N and the inflation pressure was 0.5 MPa, 0.55 MPa, and 0.6 MPa, the maximum normal grounding stress in the center of the tread was 0.978 MPa, 1.021 MPa, and 1.076 MPa, respectively. The normal grounding stresses at the tread edge were 0.759 MPa, 0.714 MPa, and 0.669 MPa, and the grounding contact areas were 0.774 m^2, 0.753 m^2, and 0.700 m^2, respectively.

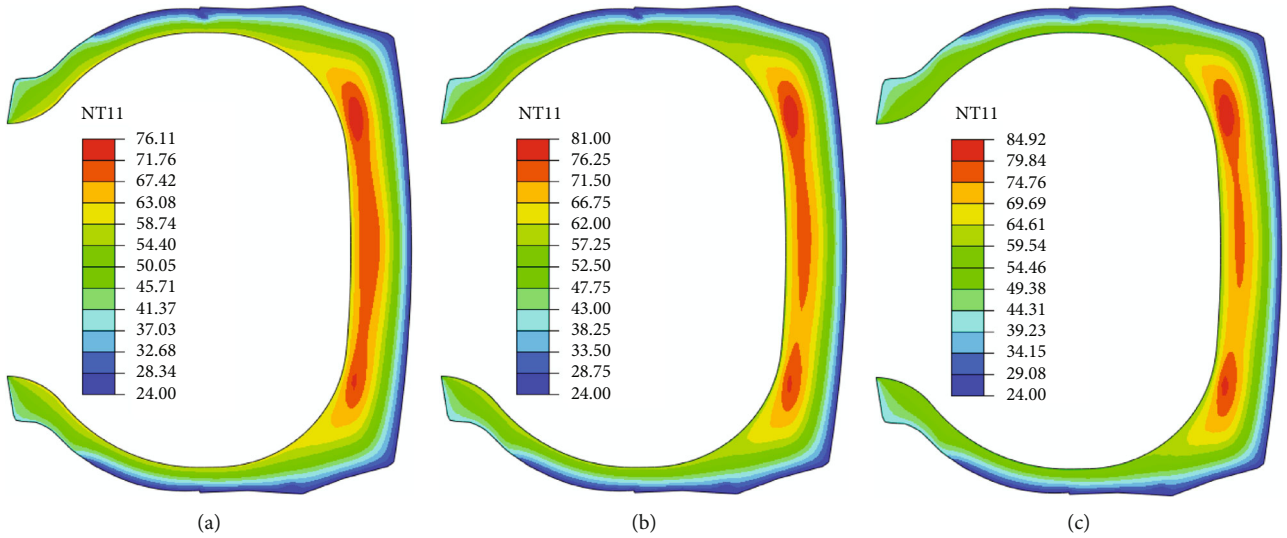

Figure 13: Temperature field distributions of a tire at a speed of 7.5 km/h: (a) 0.5 MPa inflation pressure and 46667 kg load (working Condition (1)), (b) 0.55 MPa inflation pressure and 55000 kg load (working Condition (5)), and (c) 0.6 MPa inflation pressure and 63333 kg load (working condition (9)).

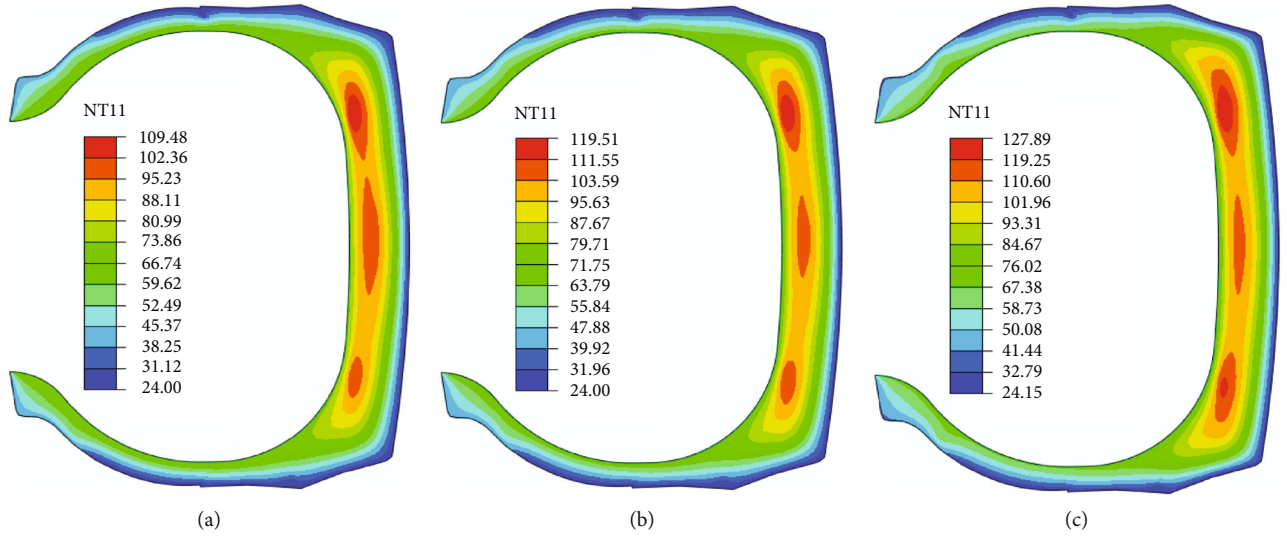

Figure 14: Temperature field distribution of a tire at a speed of 15 km/h: (a) 0.55 MPa inflation pressure and 46667 kg load (working Condition (4)), (b) 0.6 MPa inflation pressure and 55000 kg load (working condition (8)), and (c) 0.5 MPa inflation pressure and 63333 kg load (working Condition (3)).

5.2.2. Analysis of Temperature Fields. There was a correlation between the maximum temperature, charging pressure, load, and vehicle speed. To improve research efficiency and reduce the number of calculations required, intermediate variable deflection was introduced. Table 8 lists the tire deflation values under various operating conditions. Evidently, tire deflection decreased with an increase in inflation pressure and increased with an increase in load. Therefore, it is only related to inflation pressure and load, which is consistent with the trends reported in the literature [20]. Therefore, the relationships between the maximum temperature and inflation pressure, load, and vehicle speed can be transformed into a relationship between the maximum temperature, deflection, and vehicle speed. Table 8 indicates that when the vehicle speed remained constant, the maximum temperature increased in proportion to the amount of deflection. Figures 13–15 present the steady-state temperature field distributions of tires under vehicle speeds of 7.5 km/h, 15 km/h, and 22.5 km/h, respectively.

Using the range analysis method, the maximum temperature values obtained from the temperature field analysis under the nine working conditions were summarized and analyzed. This method uses the difference between the maximum and minimum values of the same factor at the different level to express the effect degree of each factor on the target result. The analysis results are presented in Table 9. K1, K2, and K3 in Table 9 represent the average values of the highest temperature of the tires in the working

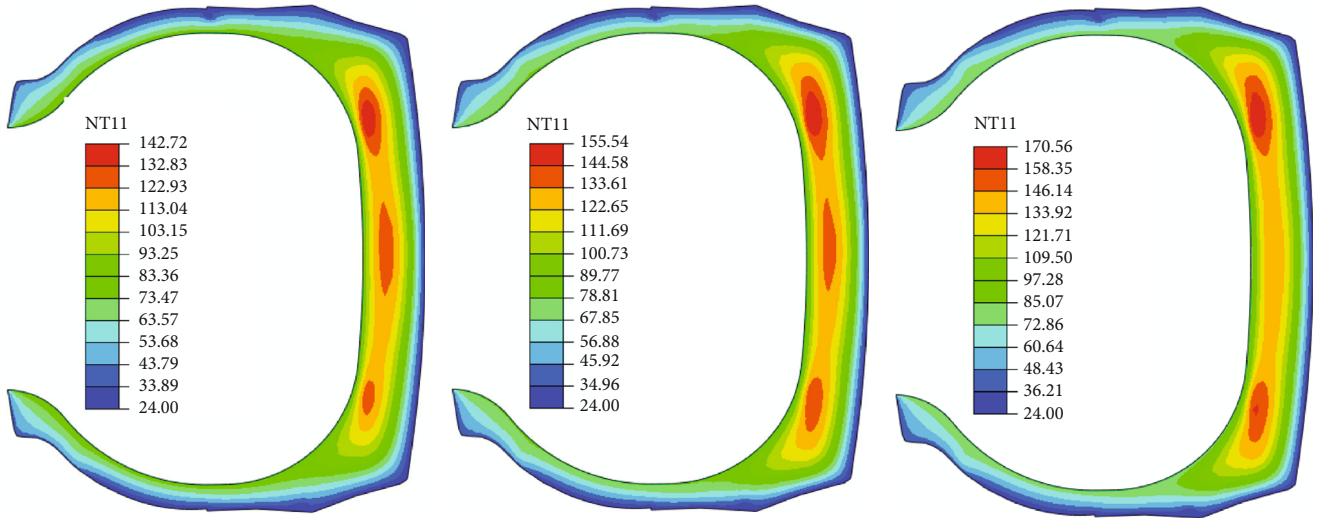

Figure 15: Temperature field distribution of a tire at a speed of 22.5 km/h: (a) 0.6 MPa inflation pressure and 46667 kg load (working Condition (7)), (b) 0.5 MPa inflation pressure and 55000 kg load (working Condition (2)), and (c) 0.55 MPa inflation pressure and 63333 kg load (working Condition (6)).

Table 9: Analysis of the range of maximum tire temperatures (°C).

Indicators	Factors		
	Inflation pressure (MPa)	Load (kg)	Velocity (km/h)
K1	119.95	109.44	80.68
K2	120.34	118.68	118.96
K3	115.72	127.79	156.27
R	4.62	18.35	75.59

conditions of the different level of each factor. The *R* value represents the difference between the maximum and minimum values among K1, K2, and K3. One can see that the *R* value relationship between the three influencing factors is R (vehicle speed) > R (load) > R (inflation pressure), indicating that vehicle speed has the greatest effect on the maximum tire temperature, followed by load and inflation pressure.

6. Conclusion

In this study, the temperature field distribution and maximum temperature of a mine tire were analyzed, and the following conclusions were drawn. A finite element model of a mine tire was developed, and the simulation results for the finite elements were compared to experimental results. The results indicated that the trends of the simulated and experimental stiffness curves were consistent with a maximum deviation of 7%. The maximum tire temperature was observed at the junction of the $1^{\#}$ belt and $2^{\#}$ belt. The temperature field simulation and experimental results showed that under the three working conditions compared, the simulated and experimental temperatures at the end of the $6^{\#}$ belt were very similar, and the maximum deviation was 6.1%. The accuracy of the finite element model was confirmed, and our method was found to be suitable for simulating large mining tires. According to our grounding analysis, grounding area decreases with increasing inflation pressure and increases with load. The maximum normal grounding stress at the center of the tread increases as the inflation pressure increases, whereas the maximum normal grounding stress at the tread edges decreases. The maximum value of normal grounding stress increases with an increase in load, and consequently, the maximum value of the normal grounding stress shifts from the center of the tread to the edge of the tread. Under 0.5 MPa, the maximum normal grounding stress increased the most with an increase in load, and 0.6 MPa increased the least. According to our analysis based on an orthogonal experimental design, tire deflection is only related to inflation pressure and load, and the maximum temperature of the tire increases as the deflection increases at the same vehicle speed. Range analysis was conducted to examine the effects of each variable on the maximum temperature. It was determined that speed had the highest impact, followed by load and inflation pressure. Overall, the results of our research indicate that it is feasible to simulate the temperature and grounding characteristics of mine tires with a high degree of accuracy. This type of analysis lays the foundation for fatigue life research at different temperatures and can be useful for designers attempting to increase the service life of mine tires while reducing costs. A limitation of this study is that the tire structure has not been improved and optimized. Therefore, promising future research directions include improving the tire structure to reduce the maximum temperature, improve the temperature distribution, and increase the service life of the tire.

Data Availability

The data used to support the findings of this study are available from the corresponding author upon request.

Conflicts of Interest

The authors declare that they have no conflicts of interest.

Acknowledgments

This study was supported by the National Natural Science Foundation of China (Grant Number 11972005), the 2021 Independent Innovation Fund of Tianjin University and Fuzhou University (Grant Number TF2021-5), the Open Fund of Fujian Key Laboratory of Force Measurement (Fujian Metrology Institute) (Grant Number FJLZSYS202102 and FJLZSYS202101), the Quanzhou Innovation and Entrepreneurship Project of High-Level Talent (Grant Number 2022C005QR), the Natural Science Foundation Projects of the Fujian Province of China (Grant Number 2021J01963), and the Quanzhou Science and Technology Plan Project (Grant Number 2020C055).

References

[1] W. Nyaaba, E. O. Bolarinwa, and S. Frimpong, "Durability prediction of an ultra-large mining truck tire using an enhanced finite element method," *Proceedings of the Institution of Mechanical Engineers, Part D: Journal of Automobile Engineering*, vol. 233, no. 1, pp. 161–169, 2019.

[2] W. Q. Zhang, "Failure simulation research of large mine electrics wheel giant tires based on ANSYS," *Automobile Parts*, vol. 11, pp. 23–26, 2015.

[3] Y. Li, S. G. Zuo, X. L. Duan, and X. L. Guo, "Test analysis of temperature field distribution of tires and its influencing factors," *Journal of Tongji University (Natural Science)*, vol. 40, no. 8, pp. 1249–1253, 2012.

[4] A. Y. Wang and W. Wang, "Simulation analysis on effect of load on heat generation of radial truck tire," *China Elastomerics*, vol. 30, no. 2, pp. 25–31, 2020.

[5] T. Tang, D. Johnson, R. E. Smith, and S. D. Felicelli, "Numerical evaluation of the temperature field of steady-state rolling tires," *Applied Mathematical Modelling*, vol. 38, no. 5-6, pp. 1622–1637, 2014.

[6] F. Li, F. Liu, J. Liu et al., "Thermo-mechanical coupling analysis of transient temperature and rolling resistance for solid rubber tire: numerical simulation and experimental verification," *Composites Science and Technology*, vol. 167, pp. 404–410, 2018.

[7] R. Behnke and R. Kaliske, "Numerical modeling of thermal aging in steady state rolling tires," *International Journal of Non-Linear Mechanics*, vol. 103, pp. 145–153, 2018.

[8] J. Marais and G. Venter, "Numerical modelling of the temperature distribution in the cross-section of an earthmover tyre," *Applied Mathematical Modelling*, vol. 57, pp. 360–375, 2018.

[9] J. Cho, H. Lee, W. Jeong, K. M. Jeong, and K. W. Kim, "Numerical estimation of rolling resistance and temperature distribution of 3-D periodic patterned tire," *International Journal of Solids and Structures*, vol. 50, no. 1, pp. 86–96, 2013.

[10] Y. J. Lin and S. J. Hwang, "Temperature prediction of rolling tires by computer simulation," *Mathematics and Computers in Simulation*, vol. 67, no. 3, pp. 235–249, 2004.

[11] F. Q. Wu, Z. R. Li, and Y. N. Xia, "Experiment and finite element analysis of steady-state temperature distribution in rolling tire under different loads and initial inflation pressures," *Engineering Mechanics*, vol. 25, no. 1, pp. 54–60, 2008.

[12] H. Yin, Y. Hu, H. Zhang, M. M. Yang, and Y. T. Wei, "Truck tire thermal-mechanical FEA and DMA with application to endurance evaluation," *Tire Science and Technology*, vol. 34, no. 4, pp. 220–236, 2006.

[13] H. S. Song, S. P. Jung, and T. W. Park, "Simulation of temperature rise within a rolling tire by using FE analysis," *Journal of Mechanical Science and Technology*, vol. 32, no. 7, pp. 3419–3425, 2018.

[14] O. H. Yeoh, "Some forms of the strain-energy function for rubber," *Rubber Chemistry and Technology*, vol. 66, no. 5, pp. 754–771, 1993.

[15] U. Nhtsa, *Department of Transportation*, National Highway Traffic Safety Administration, 2016.

[16] J. Y. Zhi, S. P. Wang, H. Q. Wang et al., "Analysis on energy loss of rubber under dynamic load," *Acta Polymerica Sinica*, vol. 4, pp. 708–715, 2017.

[17] F. Q. Wu, *Finite Element Analysis of Temperature Distribution in Steady Rolling Tires*, University of Science Technology of China, 2009.

[18] S. Ma, G. Huang, K. Obaia, S. W. Moon, and W. V. Liu, "Hysteresis loss of ultra-large off-the-road tire rubber compounds based on operating conditions at mine sites," *Proceedings of the Institution of Mechanical Engineers, Part D: Journal of Automobile Engineering*, vol. 236, no. 2-3, pp. 439–450, 2022.

[19] M. X. Huang, *The Direct Solving Strategy of Steady Tire Temperature Field and Rolling Resistance for Tire Design*, University of Science Technology of China, 2013.

[20] L. F. Yang, X. H. Wei, Y. Yin, and Y. L. Wang, "The simulation analysis on the radial tire stiffness of a aircraft," *Machinery Design & Manufacture*, vol. 5, pp. 146–148, 2013.